**PAPER** • **OPEN ACCESS**

# Interior soft x-ray tomography with sparse global sampling

To cite this article: Axel Ekman *et al* 2025 *Phys. Scr.* **100** 126008

Physica Scripta



OPEN ACCESS

RECEIVED
5 September 2025

REVISED
27 November 2025

ACCEPTED FOR PUBLICATION
2 December 2025

PUBLISHED
26 December 2025



PAPER

# Interior soft x-ray tomography with sparse global sampling

**Axel Ekman**[1,*], **Jian-Hua Chen**[1,2], **Carolyn A Larabell**[1,3], **Mark A Le Gros**[1,3] **and Venera Weinhardt**[4,5]

[1] National Center for X-ray Tomography, Lawrence Berkeley National Laboratory, Berkeley, CA, United States of America
[2] X-ray Imaging Group, Experimental Facility Division, National Synchrotron Radiation Research Center, Hsinchu 300092, Taiwan
[3] Department of Anatomy, University of California, San Francisco, San Francisco, CA, United States of America
[4] Centre for Organismal Studies, Heidelberg University, 69221 Heidelberg, Germany
[5] Institute of Microstructure Technology, Karlsruhe Institute of Technology, 76344, Eggenstein-Leopoldshafen, Germany
[*] Author to whom any correspondence should be addressed.

**E-mail:** axel.ekman@iki.fi

**Keywords:** tomography, 3D imaging, image processing

## Abstract

To investigate the feasibility of interior imaging reconstruction in soft X-ray tomography for higher-resolution cellular imaging, including whole-cell imaging, we develop an alignment and reconstruction algorithm that combines a small number of sparse whole-cell images with a high-resolution local interior scan. Based on numerical simulations, we demonstrate that combined reconstructions mitigate the depth-of-field limitation in high-resolution scans, enable radiation dose optimization, and yield quantitative X-ray absorption values with sparse sampling. We further validate our numerical approach using experimental data from two different cell types and show that the combined reconstruction reliably provides high spatial resolution within an interior region of interest of a whole cell. The resulting sparse reconstruction framework offers robust, faithful visualization of cellular organelles in soft X-ray tomography. This mesoscale imaging strategy allows one to 'scout' and zoom into selected subcellular volumes of interest, enabling increased spatial resolution without sacrificing larger-volume imaging and providing information on the relative positions of all organelles within a cell.

## 1. Introduction

Over the past years, soft X-ray tomography, or SXT, has established itself as a powerful imaging technology to tackle key questions in cell biology. To date, SXT has been used on more than 100 different cell types [1]. Several features set SXT apart from other imaging modalities. The so-called 'water-window' energy range used in SXT enables native contrast of cellular anatomy without the need for labeling or chemical fixation. This native contrast is quantitative as the X-ray linear absorption coefficient, shortly LAC, is a direct measurement of the mass density within cells [1]. Therefore, the LAC is extensively used to study the state of cellular organelles [2, 3] and mathematical modeling of their molecular composition [4]. Furthermore, SXT employs transmission geometry and computed tomography (CT) acquisition to visualize whole cells with tens of nanometers spatial resolution.

This similarity to medical CT comes along with comparable limitations. The magnification and camera pixel size limit the spatial resolution of SXT. Due to the use of diffractive X-ray optics in SXT, the increase in spatial resolution comes not only with a smaller field of view on the camera sensor but also with a shorter depth of field. Therefore, whole-cell SXT imaging with higher spatial resolution can be achieved only on smaller specimens, like bacterial cells [5]. The loss of imaging volume in high-resolution SXT can be compensated by alternative imaging geometries that combine several volumes imaged in depth [6] or by laterally expanding the field of view [7]. However, these approaches often result in higher radiation doses or loss of spatial resolution in some parts of the specimen. Therefore, the challenge of SXT imaging lies in increasing spatial resolution without compromising imaging volume or increasing the radiation dose, inevitably leading to incomplete data.

In medical CT, incomplete data is often solved by alternatives to filtered-back-projection reconstruction algorithms, such as optimal recovery, Bayes estimate, and Tikhonov-Phillips methods [8]. In a specific case where high-resolution CT scans are acquired locally, known as region of interest (ROI) tomography, the out-of-field structures affect the quantitative accuracy of the X-ray absorption coefficient and lead to artifacts, particularly at the edges of the field of view [9]. Kyrieleis *et al* [10] show that a simple extension of the truncated data can be sufficient for high-quality reconstructions using standard reconstruction methods. However, they also argued that the required sampling is still governed by the overall size of the sample, e.g., imaging a 25% ROI would require approximately a 4x increase in the number of projection images compared to the standard protocol to maintain quantitative accuracy. This approach is therefore impractical for SXT due to the resulting increase in radiation dose.

For correct quantitative reconstruction, multi-resolution approaches have been proposed, where an interior ROI CT scan is supplemented by a scout scan of a whole sample at lower resolution [11, 12]. Several interior reconstruction methods were designed to utilize the multi-resolution data. Using the low-resolution data as a prior in the reconstruction of the ROI scan [13] or re-projecting sparse views to obtain extended data for ROI scan [14] helps to reduce artifacts from data truncation and provide high-quality, reliable reconstructions of interior tomography at low computational costs.

Interestingly, the dose-fractionation theorem that is valid for biological specimens measured in computed tomography geometry[15, 16] suggests that the dose required to reconstruct a high-resolution 3D volume can be distributed among any number of different projections. Thus, an accurate reconstruction of X-ray absorption values is possible without an increase in radiation dose for such multi-resolution approaches.

Despite the broad applicability of ROI tomography in medical and laboratory CT imaging and the possibility of combining projections with no increase in radiation dose, this imaging approach has not been employed in SXT. On the one side, flat specimen supports used in some SXT instruments do not allow for full profit from multi-resolution imaging, as the samples are laterally extended. On the other hand, full-rotation SXT imaging at higher resolution is limited not only by the short depth of field, but also by the mechanical stability of the microscope [5].

Here, we develop and optimize the reconstruction algorithm, that combines sparse low-resolution and interior high-resolution SXT scans to achieve accurate and stable interior tomography in SXT. Based on theoretical considerations, we find an optimal number of low-resolution images required to obtain high-fidelity, high-resolution local imaging. To fully exploit the advantages of interior SXT, we consider full rotation over 360° and half rotation over 180° arc tomography acquisitions side by side. Furthermore, we show that dose distribution optimization in full-rotation SXT enables multi-resolution interior SXT implementation.

Finally, we probe our theoretical considerations experimentally by performing interior SXT tomography of bacteria and human B cells. Using analysis of the LAC profiles, we show that our algorithm provides a theoretically exact interior SXT reconstruction that is reliable and has great potential for cell imaging with SXT, where high and local spatial resolution is crucial, such as the substructure of small bacterial cells and membrane structures within larger human cells.

## 2. Method

Here, we present the theory and implementation of interior soft X-ray tomography in a compact form. For more details on the implementation, please see the Appendices and the GitHub repository [45]: https://github.com/ncxt/InteriorSXT

In X-ray tomography, the image formation model has traditionally been based on the Radon transform [17], the ideal linear transform (projection) of the specimen's attenuation coefficients onto a plane. This is linked to the experimental image formation through the Beer-Lambert law, such that the recorded intensity of a ray, $I_i$, can be expressed as attenuation of its intensity along a ray path, $L_i$, as

$$I_i = I_{i0} \exp\left[-\int_{L_i} \mu(t)\, \mathrm{d}t\right]. \tag{1}$$

In this work, for the inversion, we consider only the measurement in terms of a linear transform on the discrete representation of the X-ray LAC distribution $\boldsymbol{x}$ such that

$$\boldsymbol{y}_\alpha = \boldsymbol{P}_\alpha \boldsymbol{x}, \tag{2}$$

where the matrix elements $P_{\alpha ij}$ represent the contribution of $j$th voxel in the LAC distribution on the projection on the $i$th measured pixel, and $\boldsymbol{y}_\alpha$ is a vector representation of the measured absorption image $-\log \boldsymbol{I}_\alpha/\boldsymbol{I}_{\alpha 0}$.

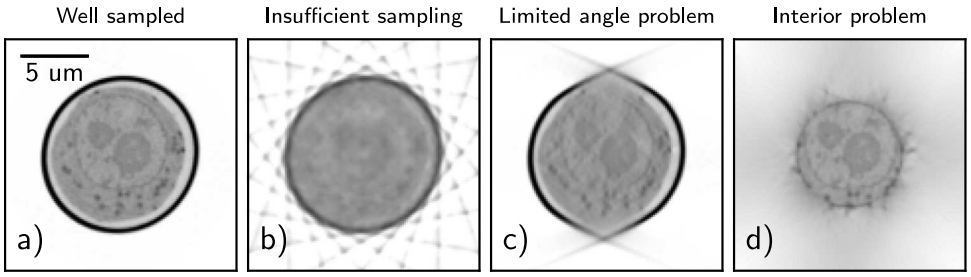


**Figure 1.** Examples of well-sampled and undetermined measurements in SXT, showing typical reconstruction artifacts arising from the nature of the forward model $\boldsymbol{A}$. a) sufficient well-sampled reconstruction with 92 projection images acquired; b) insufficient sampling, where the number of projections was reduced to 10; c) limited angle problem where 100 projections were acquired from $-65^{\circ}$ to $-65^{\circ}$, and d) interior problem where the detector width is reduced to 8 $\mu$m (from 16 $\mu$m).

A tomographic measurement can now be expressed as a series of projection operators

$$\begin{bmatrix} \boldsymbol{y}_0 \\ \vdots \\ \boldsymbol{y}_n \end{bmatrix} = \begin{bmatrix} \boldsymbol{P}_0 \\ \vdots \\ \boldsymbol{P}_n \end{bmatrix} \boldsymbol{x}, \tag{3}$$

where $\boldsymbol{P}_n$ is the measurement matrix describing the image formation of the $n$th image and $\boldsymbol{y}_n$ its corresponding absorption image. The tomographic inversion is then described by its 'measurement matrix'

$$\boldsymbol{A} := \begin{bmatrix} \boldsymbol{P}_0 \\ \vdots \\ \boldsymbol{P}_n \end{bmatrix} \tag{4}$$

[and thus, with a set of linear equations

$$\boldsymbol{A}\boldsymbol{x} = \boldsymbol{y}. \tag{5}$$

The behavior of $\boldsymbol{A}$ and the possible existence of its inverse depend on the measurement setup. In general, no unique solution exists for an overdetermined system because of noise, but suitable solutions can be found, e.g., via the normal equation

$$\boldsymbol{A}^{\top}\boldsymbol{y} = \boldsymbol{A}^{\top}\boldsymbol{A}\boldsymbol{x}, \tag{6}$$

which describes the critical points of the $l^2$-norm of the measurement errors.

The least-squares solution is not unique for an undetermined system, and the solution depends on the initial point and the reconstruction algorithm. Examples of such undetermined measurements, such as insufficient sampling, limited angle acquisition, and interior tomography, are shown in figure 1.

In X-ray tomography, the interior problem is nearly solvable, with the primary challenge being a low-frequency 'cupping' bias [18], which can be mitigated using lambda tomography [19] or by incorporating known X-ray attenuation in subregions [20].

In this study, we explore whether incorporating a sparse full field-of-view (FOV) scan can provide sufficient stabilization for the reconstruction process, particularly in high-resolution quantitative soft X-ray tomography experiments.

Specifically, we do this by extending the measurement matrix $\boldsymbol{A}_{\mathrm{ROI}}$ containing the interior scans with a set of full FOV scans $\boldsymbol{A}_{\mathrm{full}}$, such that

$$\boldsymbol{A} := \begin{bmatrix} \boldsymbol{A}_{\mathrm{ROI}} \\ \boldsymbol{A}_{\mathrm{full}} \end{bmatrix} \tag{7}$$

Our work here focuses primarily on the feasibility of the inverse problem in this setting, the sampling considerations for the SXT case, and an experimental proof of concept. Thus, all reconstructions are performed using a pure $l^2$ minimization of the measurement matrix via the conjugate gradient method on the normal equations (CGNE). For the simulated results, we determine the optimal stopping iterations based on the $l^2$ loss.

Although numerous reconstruction approaches incorporate, e.g., more accurate statistical modeling [21], regularization [22], or deep learning [23], our focus remains on the fundamental tomography model as a straightforward linear inverse problem. The formulation of the interior problem is simple and modular, and can be easily incorporated into many existing frameworks by splitting the design matrix Equation (7) into the operator-specific parts $\boldsymbol{A}_i$ for the two separate scans. For example, SIRT can be implemented as

$$x^{(k+1)} = x^{(k)} + C \odot \sum_i \boldsymbol{A}_i^{\top}(R_i \odot (y_i - \boldsymbol{A}_i x^{(k)})),$$

where $\odot$ is the Hadamard product, and

$$C = \frac{1}{\sum_i \boldsymbol{A}_i^{\top}(\mathbf{1})}, \qquad R_i = \frac{1}{\boldsymbol{A}_i(\mathbf{1})},$$

are the domain weights, and $A_i$ and $A_i^{\top}$ denote the forward and backward projection operators, respectively.

### 2.1. Null space

To assess the stability of the reconstruction within the region of interest (ROI), we evaluate its contribution to the null space of the projection operator $\boldsymbol{A}$. As discussed in [24], the domain $\mathbb{U}$ of the measurement matrix $\boldsymbol{A}$ can be divided into two subspaces, its null space $N(\boldsymbol{A})$ and its measurable space $N_{\perp}(\boldsymbol{A})$, where the null space is formally defined as

$$N(\boldsymbol{A}) = \{f \in \mathbb{U} | \boldsymbol{A}f = 0\}. \tag{8}$$

This implies that for any vector $\boldsymbol{x} \in \mathbb{U}$ that is a solution of Equation (5), then $\{\boldsymbol{x} + \boldsymbol{x}_{\text{null}}\}$ is also a solution to the equation for any vector $\boldsymbol{x}_{\text{null}} \in N(\boldsymbol{A})$. Therefore, any solution component residing in the null space does not affect the projection data and thus cannot be recovered from the measurements alone.

To estimate the null space, we follow the methods discussed in Zeng and Gullberg [25] and *Kuo et al* [24] by initializing the $\boldsymbol{x}_0$ with a phantom image. We update the image using Wilson-Barrett iterations [26]

$$\boldsymbol{x}_{n+1} = (\boldsymbol{I} - s\boldsymbol{A}^{\mathrm{T}}\boldsymbol{A})\boldsymbol{x}_n, \tag{9}$$

where $s$ is an iteration step size. From the starting point of the phantom image $\boldsymbol{x}_0 = \boldsymbol{x}_{\text{meas}} + \boldsymbol{x}_{\text{null}}$, the system can only update measurable components of $\boldsymbol{x}_0$, thus converges towards the null space component $\boldsymbol{x}_{\text{null}}$ of the phantom.

We conducted simulations with bandwidth-limited, noiseless projection images, reconstructing them using CGNE. The number of projections was selected based on the sampling requirements for a bandwidth-limited 2D Radon transform [27]. The reconstruction process was halted at the point of the highest peak signal-to-noise ratio (PSNR). In figure 2, we show both the PSNR and the relative length of the null space vector, $|\boldsymbol{x}_{null}|/|\boldsymbol{x}_0|$ for different SXT measurement setups: a full-view scan $\boldsymbol{A}_{\text{full}}$, an interior scan $\boldsymbol{A}_{\text{ROI}}$, and a combination of sparse full-view and interior scans as defined in Equation (7).

From both the reconstructions and the profiles on figure 2, we observe that the sparse scan provides a reconstruction without bias but lacks detailed resolution. While having enough sampling to capture the fine details in the truncated data, the interior scan exhibits the common artifacts associated with interior tomography. However, by combining both measurement matrices, the artifacts are corrected, and the details of a sample are preserved in reconstruction.

Furthermore, we can see that although the PSNR (and, inversely, the length of the null space vector) converges gradually when measured across the full volume, the same metrics as measured from the interior ROI stabilize rapidly with just a few full-view scans. Notably, while the matrix itself is still underdetermined, remarkably few full FOV projections are required to achieve a stable reconstruction within the ROI of the interior scan. Importantly, the LAC values of combined interior SXT reconstructions are the closest to the selected phantom.

### 2.2. PSF considerations

X-ray microscopic images are not ideal projections of objects because they are influenced by the microscope's three-dimensional point spread function (PSF) [28]. The resolution of the optical system, such as SXT, is determined by the relationship $r \propto \lambda/NA$, where $\lambda$ is the wavelength of the illuminating light and $NA$ is the numerical aperture of the objective lens. However, diffraction-limited optics impose a maximum depth of field (DOF) described by $DOF \propto \lambda/NA^2$. This narrow DOF restricts the volume in which image formation can approximate parallel projections and, particularly for large samples, may introduce radial reconstruction artifacts [29].

To address the impact of limited DOF on the accuracy of interior SXT tomography, we numerically evaluated the X-ray optics of the XM-2 microscope. The image formation process was modeled as an incoherent intensity transform, incorporating a PSF with added Poisson noise, following the approach in [29]. We analyzed two X-ray objective lenses with outer zone widths (OZW) of 35 nm and 60 nm, as described in Section Appendix A.

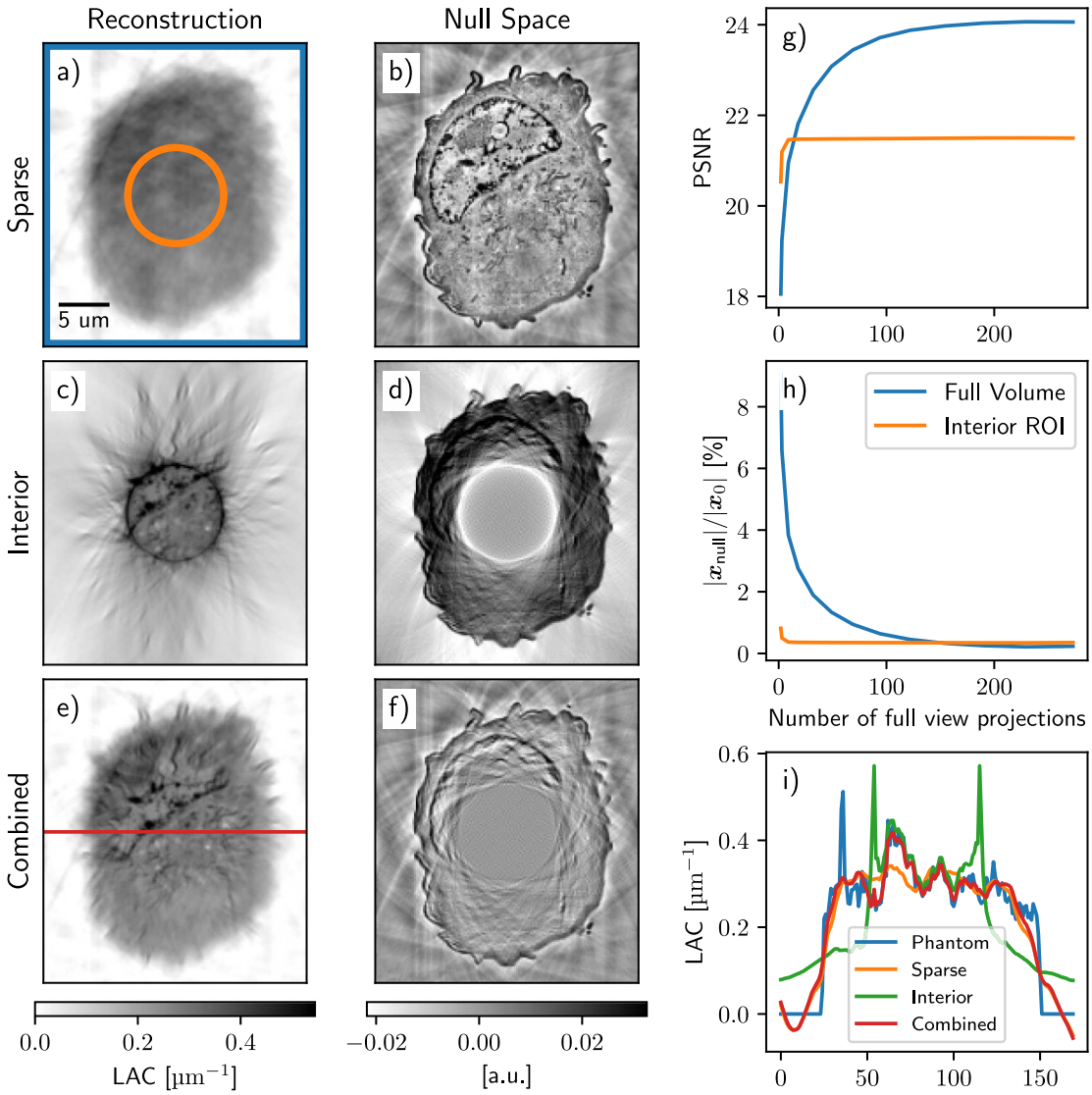


**Figure 2.** Left: Examples of reconstructions and their corresponding null space components, $\boldsymbol{x}_{\text{null}}$, (a,b) for a sparse low-resolution scan (7 projection images), (c,d) an interior scan of the same phantom (273 truncated projection images), and (e,f) a combined reconstruction of sparse low resolution and interior tomography (7 full and 273 truncated images). g) PSNR of the ROI within the interior scan (pixels within the orange circle in panel a) and the full volume (blue square shown in panel a). Both PSNRs are for the combined reconstruction as a function of the number of full-view projections used in the sparse scan. h) the relative length of the null space vector for the interior scan (orange circle in panel a) and outside ROI (orange circle). i) LAC profile across the horizontal red line shown in panel e) for the original phantom and three SXT reconstructions, which are sparse low-resolution imaging, interior high-resolution, and combined reconstructions.

To evaluate the quality of a reconstruction, $\boldsymbol{x}$, we define a relative peak signal-to-noise ratio $\text{PSNR}_{\text{rel}}$ as

$$\text{PSNR}_{\text{rel}} = \text{PSNR}(\boldsymbol{x}) - \text{PSNR}(\boldsymbol{x}_{\text{ref}}), \tag{10}$$

where $\boldsymbol{x}_{\text{ref}}$ is the 'ideal' reference reconstruction. For $\boldsymbol{x}_{\text{ref}}$, we used a high-resolution that is independent of depth (infinite DOF) and has the same lateral resolution as the 35 nm OZW.

Figure 3 presents the numerical results of Equation (10) for a 6 $\mu$m wide interior, showing variations in $\text{PSNR}_{\text{rel}}$ as a function of the radius of the cylindrical measurement region.

As expected, the PSNR and Fourier ring correction analysis (FRC) for the interior scan (in green) show that interior data preserves the high-frequency information but suffer due to bias from the truncated data, with image quality rapidly deteriorating towards the edges of the ROI. The full scan with a 35 nm OZW (in orange) scan provides better detail within the central region compared to the 60 nm OZW (in blue). For example, taking 1/7 of the resolution line in FRC analysis as a measure of spatial resolution, the in-slice resolution for full 35 nm ZP is 61 nm as compared to full 60 nm ZP with 79 nm spatial resolution.

The combined scan, using the truncated 35 nm data alongside the full 60 nm data, successfully captures the inner details of the high-resolution scan without the loss of image quality typically associated with the interior

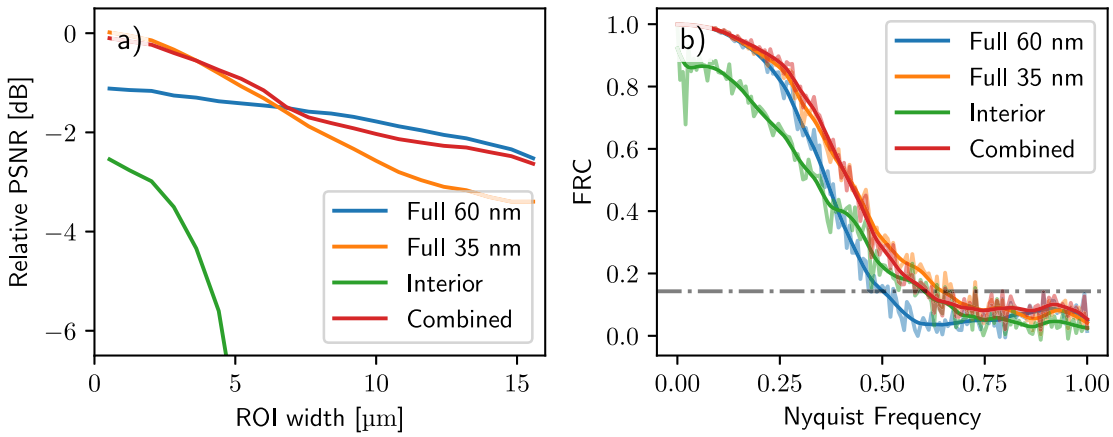


**Figure 3.** a) PSNR comparison for different scanning modes in an interior tomography setup with a 6 $\mu$m ROI. The interior scan behaves as expected. The full scan with 35 nm OZW provides better interior detail but suffers from reduced quality because of the shorter DOF. The combined scan with truncated 35 nm data and full 60 nm data preserves high inner detail without artifacts of the interior scan. b) Corresponding in-slice FRC with a ROI of 6 $\mu$m. The square ROI includes the interior boundary to exaggerate artifacts. The low-frequency bias explains the huge drop in PSNR. The multi-view protocol, including both 60 nm and 35 nm data, preserves both PSNR and FRC. The horizontal line shows the 1/7 resolution line, giving an in-slice resolution of 79 nm for the 60 nm ZP and 61 nm for the 35 nm ZP.

scan. That shows that the constraints of limited DOF go away when the interior SXT tomography is reconstructed in a combined fashion with the 'out of focus' knowledge from the sparse scan.

As shown in figure 3, the combined reconstruction of the low and high-resolution projection matrix can slightly degrade the quality of the interior scan as compared to the ideal high-resolution case. This is due to the non-optimal weight of the back-projected measurements. Using the true PSF of the microscope with its inversion [29] would mitigate this, as the back-projection weights the overlapping interior data appropriately. In practice, however, this approach is computationally costly (on the order of $N^2$, where $N$ is the width of the kernel) and suffers from slower convergence. Another solution is to apply a data-weighting scheme, as in Cao *et al* [11], to take into account the different weights of the measurement data.

We suggest approximating the projection operator as

$$\boldsymbol{A}_{\text{psf}}\boldsymbol{x} \approx \boldsymbol{k}^{*}(\boldsymbol{A}\boldsymbol{x}), \tag{11}$$

where the kernel $\boldsymbol{k}$ is a z-independent PSF and $^{*}$ the 2D convolution operator. Conversely, the adjoint operator can be expressed as

$$\boldsymbol{A}_{\text{psf}}^{\top}\boldsymbol{y} \approx \boldsymbol{A}^{\top}(\boldsymbol{k}^{\top}{*}\boldsymbol{y}). \tag{12}$$

This 2D deconvolution approach drastically speeds up the projection operator and allows it to be more easily integrated into existing projection libraries.

### 2.3. Sampling considerations

The system's optics set a physical limit on the achievable spatial resolution. However, in an experimental setup, this represents an optimistic upper limit. In reality, the spatial resolution is constrained by measurement statistics, influenced by the total radiation dose the sample can tolerate, and the specific sampling protocol used.

Dose fractionation tells us that we are free to distribute the dose in whichever way we want as long as we remain sufficiently sampled (for details, see Section B.3). However, experimentally, it is often beneficial to take fewer projections, as processing, such as alignment or deconvolution of the projection images, is much more robust. Figure 12 shows FRC analysis of conjugate gradient applied to normal equation (CGNE) reconstruction method for different angular sampling and the radiation dose. Angular sampling shows no effect on FRC curves at a lower total dose.

### 2.4. Dose optimization

Achieving high-resolution imaging with full FOV scans may require higher doses than currently used. If one is only interested in the ROI of the scan, the dose distribution of a full scan is highly non-optimal. This is illustrated in figure 4 where we show the dose distribution across a sample for three different scanning approaches: half rotation with 180° with 97 images in full FOV, full rotation 360° with 97 images in full FOV, and a combined scan with 19 full FOV images, combined with 97 interior images. For the combined scan, the

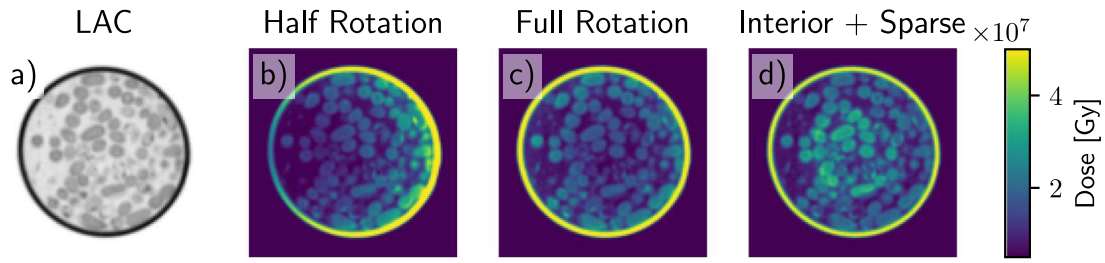


**Figure 4.** Comparison of the radiation dose distribution in a sample for different scanning protocols. a) simulated X-ray absorption (LAC) within a sample. Distribution of the dose over b) half rotation (180 degrees) c) full rotation (360 degrees), and d) the combined interior and sparse scan. The total dose on the sample for all scanning geometries is the same. The full FOV scan concentrates the dose at the sample's edges, leading to inefficient sampling. The interior scan distributes the dose more effectively within the center of the specimen.

intensity of the interior images was increased so that the total integrated dose over the entire sample matched that of the other scanning geometries.

It was previously reported [30] that the highest dose levels accumulate at the sample edges during a half-rotation FOV scan. To optimize dose distribution, the most straightforward approach is to use a full 360-degree rotation protocol. In full rotation tomography, it is essential to interlace the mirrored images such that the angular sampling is increased (if mirrored images overlap, the angular sampling is halved). Despite this, even in full-rotation scanning, a significant portion of the radiation dose is still concentrated at the sample edges and specimen holder, increasing the risk of localized radiation damage.

Going one step further, the interior SXT scan distributes the dose more effectively across the specimen, focusing on areas where detailed imaging is required. Additionally, as discussed in Section 2.1, the quality of the ROI for the combined projection operator improves rapidly with just a few full FOV scans. Beyond this point, additional full-FOV sampling provides diminishing returns regarding ROI quality while unnecessarily increasing the total radiation dose as shown in figure 2 panels g) and h).

To further investigate this trade-off, we simulated the accumulated dose in a high-resolution phantom, comparing a full scan to an interior scan while keeping the incident intensity constant. For this phantom, the average accumulated dose of a full scan, $D_{Full}$, was 2.3 times higher than that of the ROI scan, $D_{ROI}$. This means that for each full FOV image removed, the remaining dose allows for a $D_{Full}/D_{ROI}$ increase in the intensity of the interior scan while keeping the total dose constant.

To maintain consistent angular sampling for the interior scan, the redistributed dose was evenly allocated among the interior projections, leading to the following relationship:

$$I_{\mathrm{ROI}} = I_0 \frac{D_{Full}}{D_{ROI}} \frac{N_0 - N_{\mathrm{full}}}{N_0}, \tag{13}$$

where $N_0 = 499$ is the full angular sampling used as a reference.

In figure 5, we show the simulation phantom and the results of the dose optimization. As expected, while the PSNR of the full-FOV reconstruction (blue) increases with an increasing number of projection images, the quality of the combined interior scan (orange) is higher at the low number of projection images, as the dose is distributed more efficiently and results in a lower statistical error for the interior measurements. This beneficial trade breaks down at very low angular sampling (orange circle), as the number of full FOV projections is insufficient to reduce the interior bias.

Additionally, we show the result of the deconvolved reconstructions using 2D approximation as described in Equation (12). To mitigate possible inversion crimes (where both the forward model and the backward model are done with the exact same discrete operator $\boldsymbol{A}$ ), the deconvolution reconstruction was done by using a Gaussian kernel with a full-width-half-maximum equal to OZW. This deconvolution approach significantly helps to improve the quality of the combined interior scan as measured using PSNR.

Overall dose and angular sampling optimization for the phantom measurements show that a combined interior scan can be achieved with only 23 full projections. In practice, the optimal selection of dose reduction is additionally limited by experimental factors, such as alignment, which is discussed in Section Appendix B.

## 3. Experimental results

To verify the applicability of the interior SXT experimentally, we have applied our interior reconstruction method on bacteria (*Pseudomonas putida*, KT2440 strain) and human B lymphocytes (GM12878 from the NGIMS Human Genetics Cell Repository). These specimens demonstrate a variety of cells that would profit

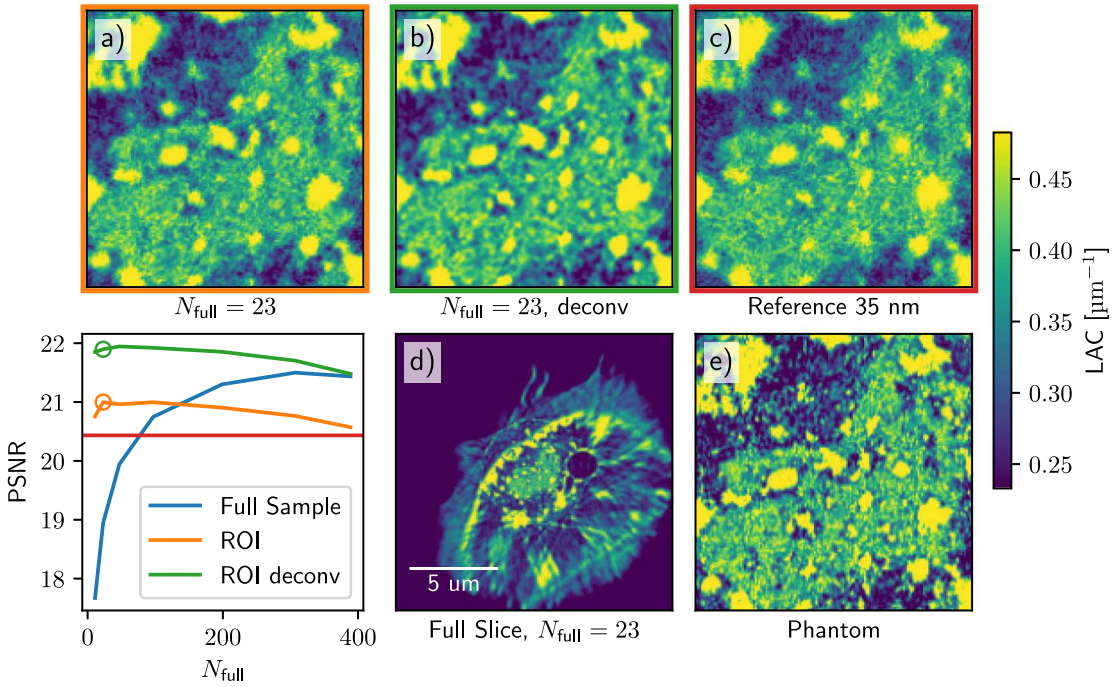


**Figure 5.** Comparison of full scan and dose-optimized scan performance. The protocols were designed so that the total dose of the sample was kept the same. The gained intensity from reducing the number of full scan images $N_{\text{full}}$ was distributed evenly across the interior scans. From the PSNR curves, we see that the overall quality decreases as the angular sampling becomes sparser, but the interior PSNR increases. The red line shows the comparison PSNR for the reference scan, i.e., a full FOV 35 nm scan with infinite DOF. At some sparse sampling, this breaks down, as the sparse measurement matrix is insufficient to reduce the interior bias in the null space. The top row shows a detail of the ROI for the peak PSNR for the direct a) and deconvolved b) reconstructions as compared to the ideal reference scan c).

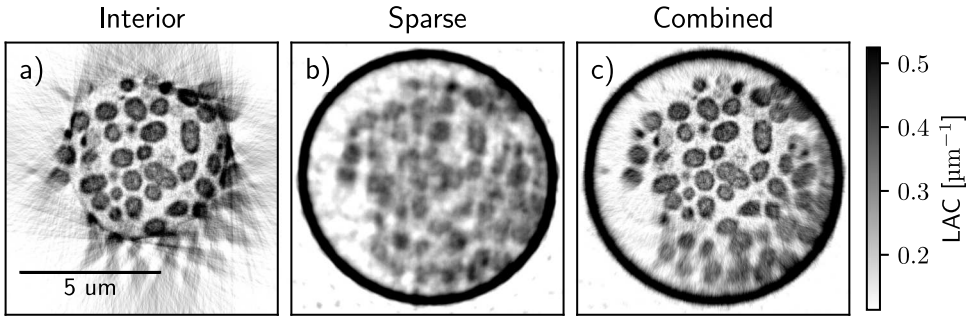


**Figure 6.** Interior SXT demonstrated experimentally on bacteria cells. Transverse virtual slices through the SXT volume for a) interior and b) sparse scans only, and c) combined reconstruction as described above. To emphasize the interior effects, the interior scan data was cropped horizontally by 25%.

from interior SXT. That is, from small cells like bacteria and yeast, where a high number of tiny cells and their structure can be quantitatively analyzed, and larger human cells, where tiny structural changes appear in an unpredictable location within the larger cell volume, are visualized in the context of other organelles and a whole cell. Like other full-rotation SXT experiments, specimens were loaded into thin-wall glass capillaries and vitrified via rapid plunging into a liquid propane [31].

For each approach, 92 projection images were acquired for full and interior tomography with 2° rotation increment and 200 ms 500 ms exposure time per projection. The projection images of full FOV and interior scans were aligned using a combination of an automatic alignment of the full FOV scans and cross-correlation of the interior projections to the full FOV data, described in detail in Section Appendix B. To demonstrate the differences in interior SXT for each cell type, we reconstruct full FOV, interior SXT, and combined reconstruction based on a full interior scan and 19 projection images from full FOV.

Figure 6 demonstrates the results obtained for an interior high-resolution scan, a sparse low-resolution SXT scan, and the combined interior tomography reconstruction. To enhance the demonstration of interior

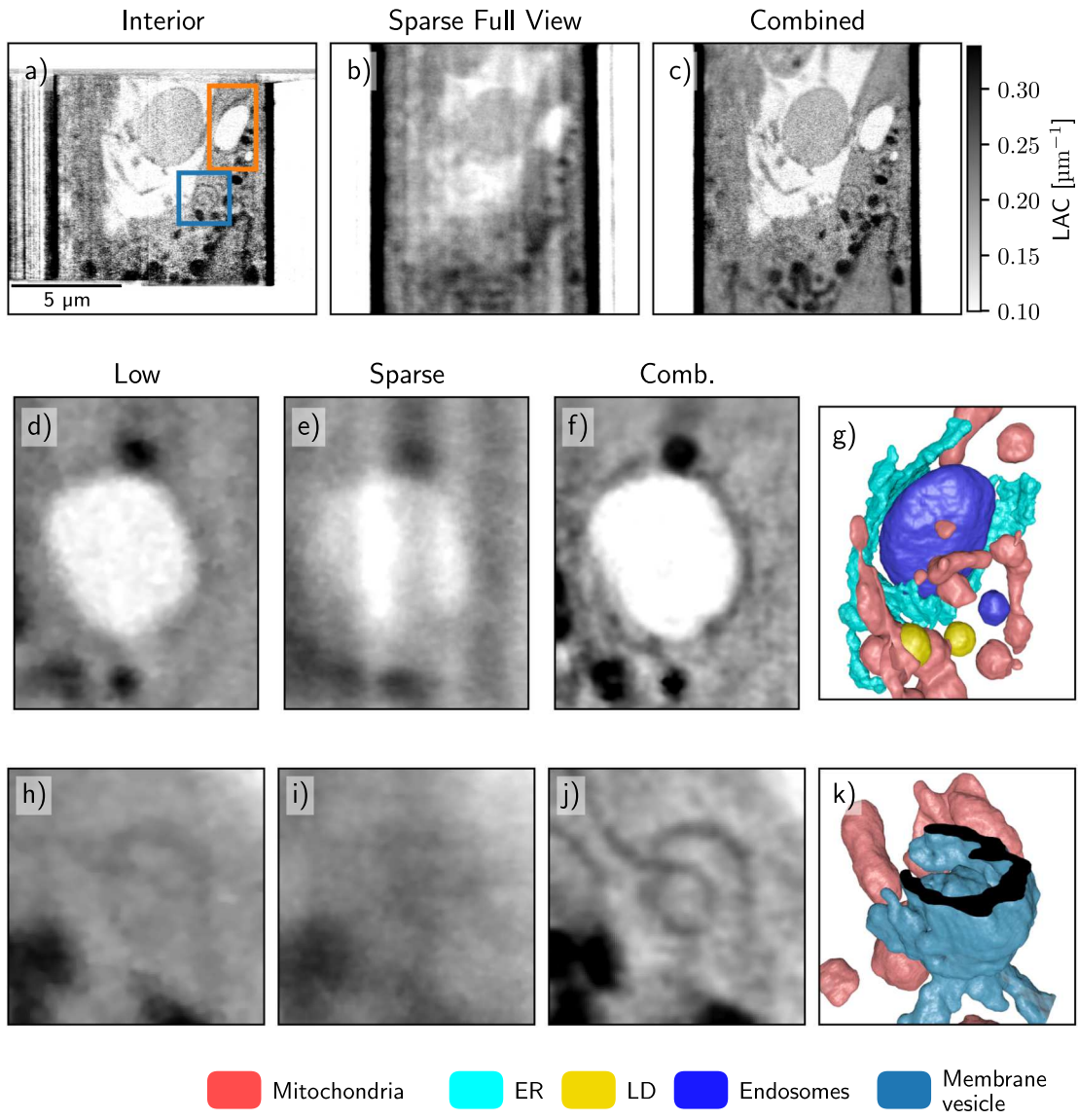


**Figure 7.** Interior SXT demonstrated experimentally on human B cells. Saggital virtual slices through the SXT volume for a) interior, b) sparse scans, and c) combined reconstruction as described above, and two highlighted ROIs. Panels (d—g) show a detailed ROI of ER wrapping around the late endosome (orange ROI in panel a). Panels (h—k) show a double membrane vesicle (blue ROI in panel a) from a low-resolution full FOV data (d and h), a sparse global sampling (e and i), and a combined interior reconstruction (f and j). Part of the outer membrane is clipped to reveal the structure inside. Panels g) and k) show 3D renderings of segmented organelles in the ROIs.

tomography, the ROI projections have been additionally cropped by 25% to reduce the FOV of the scans artificially. In-plane reconstructed virtual slices, as expected, show artifacts outside the imaging area in the interior scan. Although the interior reconstructions enable the visualization of cells inside the specimen holder, the addition of the sparse full FOV scan substantially increases the usable ROI of the reconstruction. It delivers faithful LAC reconstruction in every cell over the whole ROI as seen for cells close to the periphery of the ROI in combined with respect to interior reconstructions in figure 6.

In one such interior SXT, there are tens of individual bacterial cells, each showing variable membrane aberrations. Such subcellular changes in bacteria are of high relevance to research on genetic mutants [32], metabolism [33], and bacterial biofilms [34].

A similar comparison of the interior, sparse, and combined SXT imaging of a human B cell is shown in figure 7. All major organelles, such as the nucleus, mitochondria, and lipid droplets, are visible in all reconstruction examples. Smaller organelles, such as the endoplasmic reticulum (ER) and endosomes, are visible but challenging to segment and analyze quantitatively in sparse reconstruction. In comparison, when interior SXT is truncated with projections from full FOV, the reconstructed combined volume is free from artifacts with faithful LAC values, that are known for cellular organelles, such as mitochondria, lipid droplets and nucleus [1], and locally higher resolution.

This higher resolution region within the whole cell enables the segmentation of the region of interest (ROI1 and ROI2). Both ROIs show faint details in the low-resolution scan that could not be faithfully labeled but were segmentable semi-automatically in the combined interior scan with sparse global sampling. This type of interior high-resolution imaging enables the analysis of fine cellular features like membranes within whole human cells. Its combination with the sparse information enables a) to determine the region of interest for a 'zoom in' high-resolution SXT scan; b) to retrieve contextual information, such as proximity to the nucleus or other organelles; and c) to reconstruct faithful LAC values, enabling automatic and quantitative analysis. For the example of the ER-endosome interaction network, even just the sparse scan is sufficient to probe the position of the desired ROI, as the position of the endosome does not require high resolution or angular sampling.

Overall, the experimental results show that the combined reconstruction developed for the interior SXT scans enables the visualization of subcellular features in a large contextual volume and can be robustly used for other scientific cases.

## 4. Conclusions

In this work, we have demonstrated via the Null space of the combined projection matrix that the bias in the interior tomography vanishes when combined with sparse context scans. We showed numerically that the limitation of the shallow depth of field in the high-resolution interior scan is not relevant for the combined reconstructions, as the sparse scan provides the 'out of focus' information. Furthermore, based on the dose fractionation theorem, we argue that since SXT imaging is primarily noise-limited, optimizing the dose distribution is more critical than increasing angular sampling. The calculated dose distribution confirms that the combined interior SXT reconstruction utilizes the radiation dose more effectively within the specimen holder than half- and full-rotation tomography.

In practice, the optimal selection of imaging is limited by experimental factors, such as alignment. We, therefore, performed multi-resolution imaging of bacteria and human B cells. Based on these experimental data, we show that combined reconstructions of the interior SXT enable faithful reconstructions of LAC values in 3D. For small cells like bacteria or yeast, our combined reconstructions allow for analysis of subcellular alterations for tens of cells. Conversely, combined interior reconstructions required only 19 projections from the sparse scan. That enables us to perform low-resolution 'scout' SXT imaging, followed by a zoom-in into the region of interest in larger cells, like human B cells. Therefore, the combined reconstruction of the interior SXT imaging is a valuable tool for several application cases.

Our combined reconstruction algorithm of interior tomography provides numerical consideration and the first experimental evidence that the resolution limit in SXT imaging can be increased without sacrificing larger-volume imaging.

## Acknowledgments

Soft X-ray tomography was conducted at the National Center for X-ray Tomography, which is supported by NIH NIGMS (grant no. P30GM138441) and the Department of Energy's Office of Biological and Environmental Research (grant no. DE-AC02-5CH11231). V.W.'s work was funded by the Heisenberg program of the German Research Foundation (WE 6221/6-1), by the CLEXM MSCA-DN project funded by the European Union under Horizon Europe, and by the NanoX project (101167089) funded by the European Research Council (ERC) under the European Union's Horizon Europe research and innovation programme.

## Data availability statement

All data that support the findings of this study are included within the article (and any supplementary files) [45].

## Appendix A. Simulation

For a high-resolution phantom, we used a Macrophage cell (jrc_macrophage-2) from OpenOrganelle [35]. The Linear Attenuation Coefficient (LAC) values were approximated by measuring the mean gray values from the provided label field. These values were then linearly scaled to match the known LAC values of the respective organelles. The average LAC for the phantom was approximately 0.28 $\mu m^{-1}$.

Figure 2 used a downsampled image of shape 196 px $\times$ 170 px. For figures 3, 5, and 12, the phantom was cropped to a circular ROI of width 801 px, with a pixel size of 20 nm.

For bandwidth-limited projections, we used the linearized incoherent model for the forward model as previously described [29]. The high-resolution and low-resolution PSFs were approximated by modeling the MZP as an ideal circular lens, with the effective PSF calculated according to the methods outlined previously [36], by the converging illumination emerging from a circular lens aperture based on the Huygens-Fresnel principle [37].

The MZPs used in the simulations had outer zone widths (OZW) of 35 nm and 60 nm for high and low-resolution setups, respectively. These parameters were chosen to simulate the current configuration at the XM-2 microscope. In XM-2 [38], the condenser is configured as a linear monochromator, formed by the condenser zone plate and a pinhole placed close to the specimen, meaning that we have the same effect of elongated PSF as described in [36]. We have chosen a representative wavelength from the 'water window' of 2.4 nm with a monochromaticity of $\lambda_0/\Delta\lambda = 300$. As an 'ideal' reference, we used a z-independent PSF equal to the focal point of the 35 nm OZW. For the Beer-Lambert model's forward and backward projection operators, we used the ASTRA toolbox [39–41] via Tomosipo [42].

As the phantom's variability in thickness was high, we used a z-normalizing flat field as the illumination profile so that a single Poisson noise level could better describe the images. This was done by taking an ideal Beer-Lambert projection of the sample and then averaging all illumination profiles over the mean horizontal absorption of the sample.

The approximate noise level of the PSNR was measured from diagonally split experimental data. A similar measurement was done on PSF simulated projections to extract the necessary Poisson count for similar PSNR, with a result of about 150 photons / $(10\ \text{nm})^2$.

Code available at https://github.com/ncxt/InteriorSXT. [45]

## Appendix B. Experimental results

### B.1. Alignment

The alignment is preceded by the alignment of the full-FOV stack following standard protocol [31] using AREC3D [43]. Since the entire sample is within the field of view, pre-aligning the capillary using a rigid body transformation is highly robust, even in cases of sparse sampling. The aligned stack is then upscaled to match the resolution of the high-resolution interior projection images.

These images (anchors) $\boldsymbol{A}_i$ serve as accurately aligned reference images for the interior scan. A schematic representation of the alignment setup is shown in figure 8. Note that the mirror images can also be used as anchor points for sampling protocols spanning over 180°.

We seek translations $T_i$ to the interior images $\boldsymbol{I}_i$, that maximises the function

$$\arg\max_{T_i}\left(\sum_{C_a} f\left(T_i I_i,\ A_j\right) + \sum_{C_{nn}} f\left(T_i I_i,\ T_j I_j\right)\right) \tag{14}$$

where $C_a$ is the collection of image-anchor pairs $i, j$, for which the angular difference to the anchor is smaller than half of that to its nearest neighbor, and $C_{nn}$ is the collection of nearest neighbor image-image pairs.

As an alignment metric $f$, we used the normalized cross-correlation

$$NCC(\boldsymbol{x},\ \boldsymbol{y}) = \frac{\Sigma_i (x_i - \bar{\boldsymbol{x}})(y_i - \bar{\boldsymbol{y}})}{\sqrt{\Sigma (x_i - \bar{\boldsymbol{x}})^2}\sqrt{\Sigma (y_i - \bar{\boldsymbol{y}})^2}}\ , \tag{15}$$

where $\boldsymbol{x}$ and $\boldsymbol{y}$ are vector representations of the overlapping information of the two images and $\bar{\boldsymbol{x}}$, $\bar{\boldsymbol{y}}$, their respective means.

The alignment of the interior images was initially set using a nearest-neighbor approach. A global shift was determined for all images based on reliable full-scan anchor points. This shift was then smoothly interpolated to provide an initial estimate for the interior alignment across the whole dataset. Starting from this initial alignment, the alignment function Equation (14) was optimized using Quasi-Newton methods [44].

Values of $NCC(\boldsymbol{x}, \boldsymbol{y})$ were only evaluated at integer shifts, and intermediate values were obtained by bicubic interpolation. This way, cached values of integer shifts for $NCC$ were used to obtain both function values and their derivatives of sub-pixel shifts.

Pure nearest-neighbor alignment generally fares relatively poorly in tomography, as there can be substantial drift in successive alignments. The anchor points (shown in figure 8) mitigate this, as it reduces the length of long chains where this drift can happen.

To investigate how many such anchors are experimentally needed for faithful alignment of the interior data, several alignments were performed using only a sparse subset of the complete low-resolution dataset. Figure 9 presents the mean alignment error $|T_i - T_i^{\text{ref}}|$ ($L_2$ norm) as a function of anchor sparsity for experimental bacteria and B-cell datasets, where $T_i^{\text{ref}}$ are the interior translations using all available full FOV images

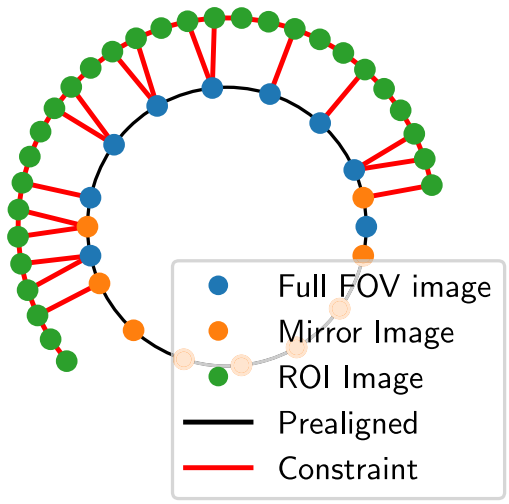


**Figure 8.** Schematic graph of the alignment procedure. The nodes represent the images, while the edges represent the transformation between them. The inner circle shows the fixed transformation of the pre-alignment, while the outer circle represents the nearest neighbor of the interior scan. An auxiliary constraint is added to a pre-aligned anchor image for an interior image when its angular distance is smaller than that to its nearest neighbor.

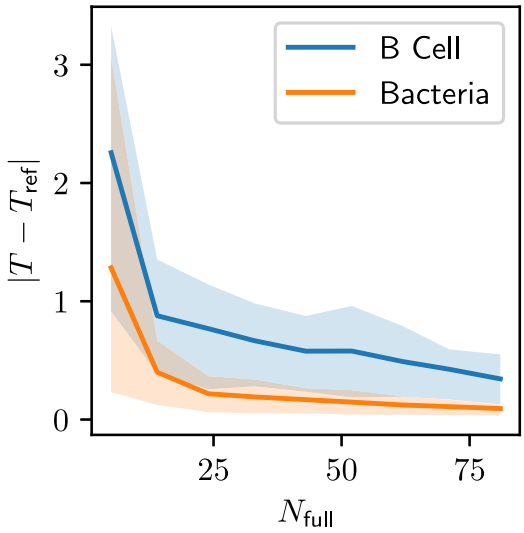


**Figure 9.** Mean length $|T_i - T_I^{\text{ref}}|$ of the alignment difference between sparse reference data for B cell and Bacteria as a function of anchor sparsity. The shaded area shows the $\pm\sigma$ percentile.

as anchor points. The results demonstrate a slow quality decay (sub-pixel accuracy) with reduced full-FOV images to as low as 10 images, where the alignment error increases significantly.

Optimal sampling should balance the number of anchor points with alignment stability and dose. Too few anchors lead to significant drift, while excessive anchors introduce sub-optimal dose distribution. Notably, interleaved sampling plays a crucial role in reducing systematic biases by ensuring that mirror images contribute distinct anchor points, thereby enhancing the robustness of the alignment procedure.

### B.2. Note on absorption correction

For both 60 nm and 35 nm OZW objectives, the same monochromator setup is used. In this scenario, a higher-order diffraction of an incoming X-ray beam could be potentially focused on the sample. To account for this potential contamination of X-ray absorption values, we use a dual-energy model to correct the transmission values of the experimental data between sparse and interior scans.

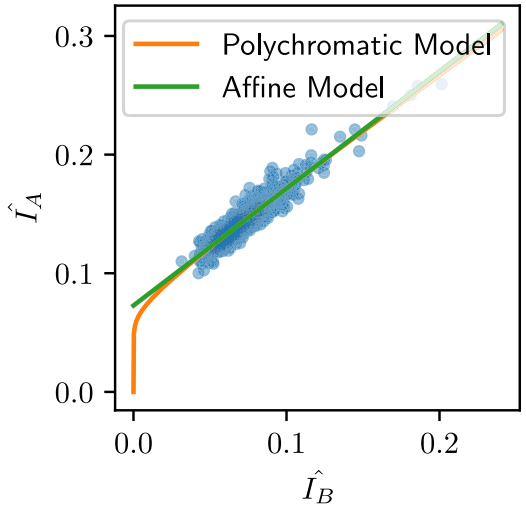


**Figure 10.** An example of the fitted intensity transform between the 60 nm and the 35 nm images. The orange line shows the used transformation using the polychromatic model of Equation (16). The green line shows a simple affine model, where the intensity difference is caused by unspecified stray light.

The low-resolution intensity is modeled as pure monochromatic Beer-Lambert

$$\hat{I_A} = \mathrm{e}^{-\mu L}.$$

For the high-resolution MZP, we model the intensity as a dual-energy setup, where the intensity is now given by

$$\hat{I_B} = \{\phi_0 \mathrm{e}^{-\mu_0 L} + \phi_1 \mathrm{e}^{-\mu_1 L}\},$$

where $\phi_0$ and $\phi_1$ are the relative intensities of the two energies. As the LAC is energy dependent, we should also describe the sample with two different absorption coefficients $\mu_0$ and $\mu_1$. For the sake of simplicity, we assume that the dependency between absorption and energy can be described as a linear function $\mu_2 = c\mu_1$.

With this approximation, the intensity of the high-resolution scan can be described as

$$\hat{I_B} = \phi_0 \hat{I_A} + (1 - \phi_0)\hat{I_A}^c \tag{16}$$

In figure 10, we show the best fit of model Equation (16) to the collected normalized data for the Bacteria sample and compare it to a simple affine model for stray light.

### B.3. Note on bandwidth-limited sampling of the Radon transform

For this, we consider the Radon transform of a two-dimensional impulse function as described by Rattey and Lindgren [27]. We can express its Radon transformation as

$$P(\omega_\theta, \omega_u) = 2\pi \mathrm{e}^{-j\omega_t(\pi/2+\phi_0)} J(\omega_t, r_0\omega_t), \tag{17}$$

where $(r_0, \phi_0)$ is the position of the impulse function in polar coordinates, $\omega_\theta$ and $\omega_u$ are the angular and positional frequency, respectively, and the angular frequency $\omega_\theta \in \mathbb{Z}$ and only takes discrete values.

In a discrete setting where we take the Radon transform for a single voxel of LAC $\mu$, this is equivalent to

$$P(k_\theta, k_u) = \mu N_\mathrm{a} \phi_\theta \phi_u J(k_\theta, 2\pi R/Lk_u) \tag{18}$$

where $\phi_\theta$ and $\phi_u$ are the appropriate phase shifts for the angular and positional sampling, $N_a$ the number of angles, and $k_\theta = -N_a/2 \ldots N_a/2$ and $-L/2 \ldots L/2$.

The function $|J(x, y)|$ approaches zero as $x \gg y$, forming a structure that resembles an 'infinite length bowtie' [27]. For the bandwidth-limited case, we multiply the columns by the OTF,

$$F_{otf}(k_\theta, k_u) = OTF(k_\theta) F(k_\theta, k_u) \tag{19}$$

Next, we can investigate the total power collected from different sampling schemes. Integrating the cumulative spectral power of the signal $|F_{otf2}|^2$ with respect to $k_\theta$, we can quantify the amount of signal power collected by the limited sampling compared to the 'ideal case'. In figure 11 we an example of the OTF limited Radon transform for the 60 nm OZW and the cumulative power for both 35 nm and 60 nm OZW, showing that most of the signal is collected with sparse sampling while capturing the remaining power requires increasingly dense angular sampling. The sampling limit of $N_a \approx (2\pi R f_{\mathrm{cut}})$ is shown in figure 11(a), where the spatial frequency $f_{\mathrm{cut}}$ was chosen to correspond to 98% of the OTF power.

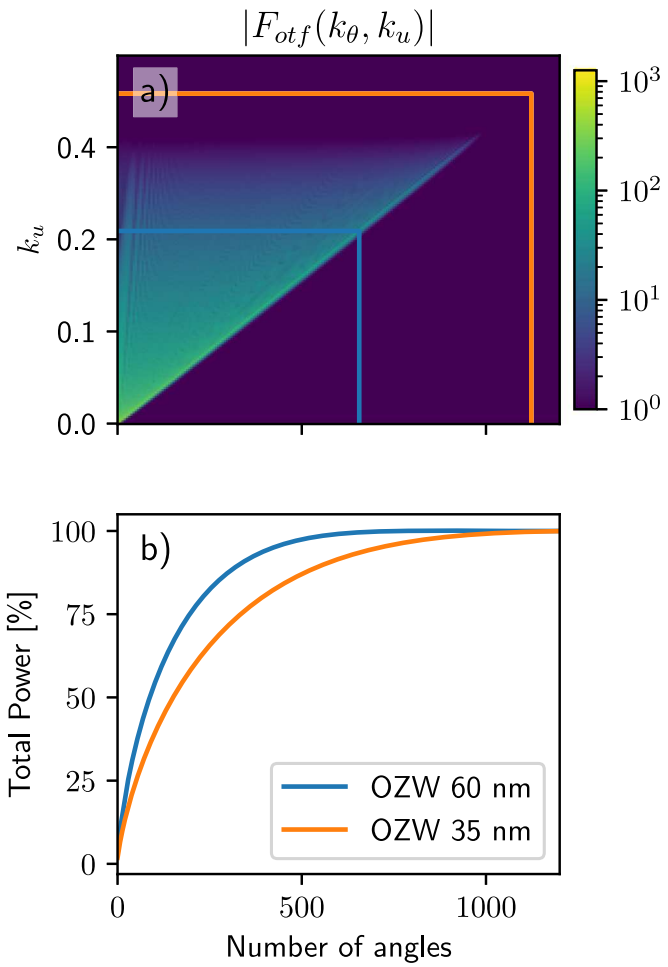


**Figure 11.** a) A quadrant of the function $|F_{otf}(k_\theta, k_u)|$ showing bandwdth-limited bowtie of the 60 nm OZW. The blue and orange lines show the accurate sampling up to 98 % of the OTF power for the 60 nm (656 images) and 35 nm (1256) ZP. b) Integrated total power of the signal with respect to the angular sampling as described in Section B.3. $L = 800$ $r = 400$ sampled with a grid pixel size of 20 nm.

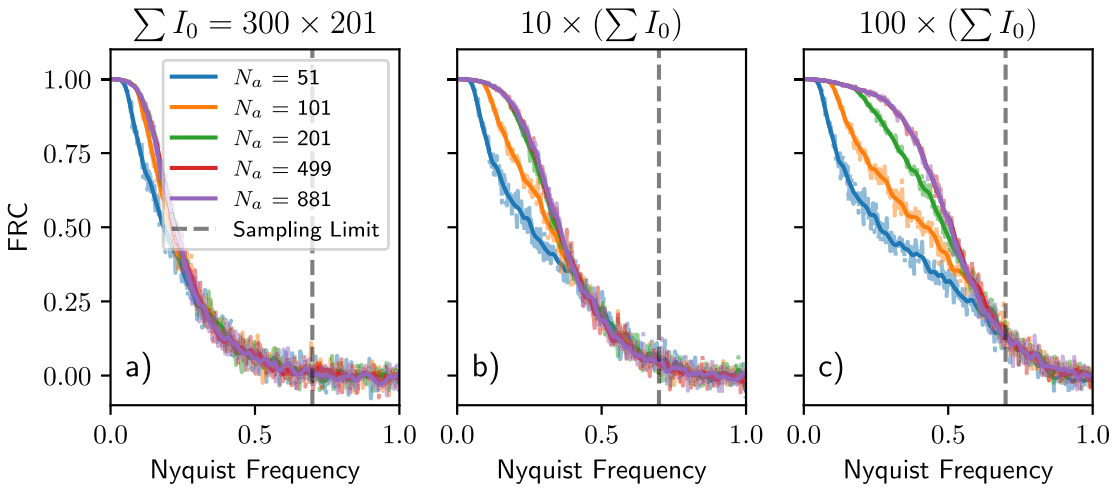


**Figure 12.** In-slice FRC reconstructions for different angular sampling rates. Sampling limit shows the theoretical resolution limit based on the Radon sampling at $N_a = 881$. At lower total doses, dose fractionation holds for sampling rates well below the standard sampling criterion. As the total dose increases, the effects of sparse sampling become more pronounced. However, these deviations require both higher dose and sparser sampling than is commonly employed.

We argue that when the imaging scheme becomes highly noise-limited, the importance of dense angular sampling diminishes, as the SNR of the highest-frequency components degrades. In figure 12, we present three examples of sampling with equal total dose. At the lowest dose, no effect of sparse sampling is observed. As the dose increases, the impact of sparse sampling becomes apparent, particularly in cases with the lowest angular sampling densities.

## Author contributions

Jian-Hua Chen 0000-0002-7998-0878
Data curation (equal), Investigation (equal), Methodology (equal), Resources (equal), Writing – review & editing (equal)

Venera Weinhardt 0000-0002-9774-3833
Conceptualization (equal), Data curation (equal), Formal analysis (equal), Investigation (equal), Methodology (equal), Visualization (equal), Writing – original draft (equal), Writing – review & editing (equal)

## References

[1] Weinhardt V and Larabell C 2025 Soft x-ray tomography has evolved into a powerful tool for revealing cell structures *Annual Review of Analytical Chemistry* **18** 427–446
[2] Le Gros M A, Clowney E J, Magklara A, Yen A, Markenscoff-Papadimitriou E, Colquitt B, Myllys M, Kellis M, Lomvardas S and Larabell C A 2016 Soft x-ray tomography reveals gradual chromatin compaction and reorganization during neurogenesis in vivo *Cell Reports* **17** 2125–36 https://www.sciencedirect.com/science/article/pii/S2211124716314802
[3] Hanssen E, Knoechel C, Dearnley M, Dixon M W A, Le Gros M, Larabell C and Tilley L 2012 Soft x-ray microscopy analysis of cell volume and hemoglobin content in erythrocytes infected with asexual and sexual stages of plasmodium falciparum *J. Struct. Biol.* **177** 224–32 https://www.sciencedirect.com/science/article/pii/S1047847711002589
[4] Autin L, Barbaro B A, Jewett A I, Ekman A, Verma S, Olson A J and Goodsell D S 2022 Integrative structural modelling and visualisation of a cellular organelle *QRB discovery* **3** e11
[5] Weinhardt V *et al* 2020 Switchable resolution in soft x-ray tomography of single cells *PLoS One* **15** e0227601
[6] Otón Joaquín *et al* 2017 Xtend: Extending the depth of field in cryo soft x-ray tomography *Sci. Rep.* **7** 45808
[7] Ekman A, Chen J-H, Vanslembrouck B, Loconte V, Larabell C A, Le Gros M A and Weinhardt V 2023 Extending imaging volume in soft x-ray tomography *Advanced Photonics Research* **4** 2200142
[8] Natterer F and Hadeler K P 1980 Efficient implementation of 'optimal'algorithms in computerized tomography *Math. Methods Appl. Sci.* **2** 545–55
[9] Gore J C and Leeman S 1980 The reconstruction of objects from incomplete projections *Physics in Medicine & Biology* **25** 129
[10] Kyrieleis A, Titarenko V, Ibison M, Connolley T and Withers P J 2011 Region-of-interest tomography using filtered backprojection: assessing the practical limits *J. Microsc.* **241** 69–82
[11] Cao Q, Zbijewski W, Sisniega A, Yorkston J, Siewerdsen J H and Stayman J W 2016 Multiresolution iterative reconstruction in high-resolution extremity cone-beam ct *Physics in Medicine & Biology* **61** 7263
[12] Dang H, Stayman J W, Sisniega A, Zbijewski W, Xu J, Wang X, Foos D H, Aygun N, Koliatsos V E and Siewerdsen J H 2016 Multi-resolution statistical image reconstruction for mitigation of truncation effects: application to cone-beam ct of the head *Physics in Medicine & Biology* **62** 539
[13] Luo S, Shen T, Sun Y, Li J, Li G and Tang X 2018 Interior tomography in microscopic ct with image reconstruction constrained by full field of view scan at low spatial resolution *Physics in Medicine & biology* **63** 075006
[14] Sharma K S, Holzner C, Vasilescu Dragoş M, Jin X, Narayanan S, Agah M, Hoffman E A, Yu H and Wang G 2013 Scout-view assisted interior micro-ct *Physics in Medicine & Biology* **58** 4297
[15] Hegerl R and Hoppe W 1976 Influence of electron noise on three-dimensional image reconstruction *Zeitschrift für Naturforschung A* **31** 1717–21
[16] McEwen B F, Downing K H and Glaeser R M 1995 The relevance of dose-fractionation in tomography of radiation-sensitive specimens *Ultramicroscopy* **60** 357–73
[17] Radon Johann 1917 Über die Bestimmung von Funktionen durch ihre Integralwerte längs gewisser Mannigfaltigkeiten *Berichte über die Verhandlungen der Königlich-Sächsischen Gesellschaft der Wissenschaften zu Leipzig. Mathematisch-Physische Klasse* **69** 262–77
[18] Maass P 1992 The interior radon transform *SIAM J. Appl. Math.* **52** 710–24
[19] Faridani A, Ritman E L and Smith K T 1992 Local tomography *SIAM J. Appl. Math.* **52** 459–84
[20] Courdurier M, Noo Frédéric, Defrise M and Kudo H 2008 Solving the interior problem of computed tomography using a priori knowledge *Inverse Problems* **24** 065001
[21] Jeffrey A, Fessler M and Sonka J M 2000 Fitzpatrick. Statistical image reconstruction methods for transmission tomography *Handbook of medical imaging* **2** 1–70
[22] Zhang H, Wang J, Zeng D, Tao X and Ma J 2018 Regularization strategies in statistical image reconstruction of low-dose x-ray ct: A review *Med. Phys.* **45** e886–907
[23] Szczykutowicz T P, Toia G V, Dhanantwari A and Nett B 2022 A review of deep learning ct reconstruction: concepts, limitations, and promise in clinical practice *Current Radiology Reports* **10** 101–15
[24] Kuo J, Granstedt J, Villa U and Anastasio M A 2022 Computing a projection operator onto the null space of a linear imaging operator: tutorial *J. Opt. Soc. Am. A* **39** 470–81
[25] Zeng G L and Gullberg G T 2012 Null-space function estimation for the interior problem *Physics in Medicine & Biology* **57** 1873
[26] Wilson D W and Barrett H H 1998 Decomposition of images and objects into measurement and null components *Opt. Express* **2** 254–60
[27] Rattey P and Lindgren A 1981 Sampling the 2-d radon transform *IEEE Trans. Acoust. Speech Signal Process.* **29** 994–1002

[28] Oton J, Sorzano C O S, Pereiro E, Cuenca-Alba Jesús, Navarro R, Carazo J M and Marabini R 2012 Image formation in cellular x-ray microscopy *J. Struct. Biol.* **178** 29–37
[29] Ekman A, Weinhardt V, Chen J-H, McDermott G, Le Gros M A and Larabell C 2018 Psf correction in soft x-ray tomography *J. Struct. Biol.* **204** 9–18
[30] Loconte V, Chen J-H, Cortese M, Ekman A, Le Gros M A, Larabell C, Bartenschlager R and Weinhardt V 2021 Using soft X-ray tomography for rapid whole-cell quantitative imaging of SARS-CoV-2-infected cells *Cell Reports Methods* 100117 https://www.sciencedirect.com/science/article/pii/S2667237521001818
[31] Chen J-H, Vanslembrouck B, Loconte V, Ekman A, Cortese M, Bartenschlager R, McDermott G, Larabell C A, Le Gros M A and Weinhardt V 2022 A protocol for full-rotation soft x-ray tomography of single cells *STAR protocols* **3** 101176
[32] Cossa A, Trépout S, Wien F, Groen J, Le Brun E, Turbant F, Besse L, Pereiro E and Arluison Véronique 2022 Cryo soft X-ray tomography to explore Escherichia coli nucleoid remodeling by Hfq master regulator *J. Struct. Biol.* **214** 107912 https://www.sciencedirect.com/science/article/pii/S104784772200082X
[33] Eng T *et al* 2023 Maximizing microbial bioproduction from sustainable carbon sources using iterative systems engineering *Cell Reports* **42** (9) 113087
[34] Chatzimpinou A *et al* 2025 Soft X-ray tomography reveals variations in B. subtilis biofilm structure upon tasA deletion *npj Biofilms and Microbiomes* 11, 1–10 https://www.nature.com/articles/s41522-025-00659-0 (Nature Publishing Group)
[35] Heinrich L *et al* 2021 Whole-cell organelle segmentation in volume electron microscopy *Nature* **599** 141–6
[36] Weiss D, Schneider G, Niemann B, Guttmann P, Rudolph D and Schmahl G 2000 Computed tomography of cryogenic biological specimens based on x-ray microscopic images *Ultramicroscopy* **84** 185–97
[37] Born M and Wolf E 1970 *Principles of optics: electromagnetic theory of propagation, interference and diffraction of light* (Pergamon Press)
[38] Le Gros M A, McDermott G, Cinquin B P, Smith E A, Do M, Chao W L, Naulleau P P and Larabell C A 2014 Biological soft x-ray tomography on beamline 2.1 at the advanced light source *J. Synchrotron Radiat.* **21** 1370–7
[39] Aarle W V, Palenstijn W J, Beenhouwer J D, Altantzis T, Bals S, Batenburg K J and Sijbers J 2015 The astra toolbox: A platform for advanced algorithm development in electron tomography *Ultramicroscopy* **157** 35–47
[40] Aarle W V, Palenstijn W J, Cant J, Janssens E, Bleichrodt F, Dabravolski A, Beenhouwer J D, Batenburg K J and Sijbers J 2016 Fast and flexible x-ray tomography using the astra toolbox *Opt. Express* **24** 25129–47
[41] Palenstijn W J, Batenburg K J and Sijbers J 2011 Performance improvements for iterative electron tomography reconstruction using graphics processing units (gpus) *J. Struct. Biol.* **176** 250–3
[42] Hendriksen A, Schut D, Palenstijn W J, Viganò N, Kim J, Pelt Daniël, van Leeuwen T and Joost Batenburg K 2021 Tomosipo: Fast, flexible, and convenient 3D tomography for complex scanning geometries in Python *Opt. Express* (https://doi.org/10.1364/oe.439909)
[43] Parkinson D Y, Knoechel C, Yang C, Larabell C A and Le Gros M A 2012 Automatic alignment and reconstruction of images for soft x-ray tomography *J. Struct. Biol.* **177** 259–66
[44] Virtanen P *et al* 2020 and SciPy 1.0 Contributors. SciPy 1.0: Fundamental Algorithms for Scientific Computing in Python *Nat. Methods* **17** 261–72
[45] Ekman A *et al* 2025 Interior soft X-ray tomography with sparse global sampling: code and data (https://doi.org/10.5281/zenodo.18009677)